

EXPERIMENTAL STUDY ON BEARING CAPACITY OF AUSTENITIC STAINLESS STEEL LIPPED CHANNEL COLUMNS

Sheng-gang Fan ^{1,*}, Run-min Ding ¹, Yun-long Han ², Mei-he Chen ¹, Cheng-liang Liu ³ and Yue-lin Tao ³

¹ Key Laboratory of Concrete and Prestressed Concrete Structures of Ministry of Education, School of Civil Engineering, Southeast University, Nanjing, China

² Architectural Design and Research Institute Co. Ltd. of Southeast University, Nanjing, China

³ East China Architectural Design & Research Institute Co. Ltd., Shanghai, China

* (Corresponding author: E-mail: 101010393@seu.edu.cn)

ABSTRACT

An experimental program was conducted to study the bearing capacity of austenitic stainless steel lipped channel columns subjected to axial and eccentric compression in this paper. 14 tensile austenitic AISI304 stainless steel tensile coupons were tested to obtain the material properties of the flat and the corner zones of the specimens. The tensile test results show nonlinear stress-strain behaviour with low proportionality limit, anisotropy and strength enhancement because of cold working. To supplement the experimental data on stainless steel lipped channel members, 24 specimens in all were carried out, including 6 axially compressed columns and 18 eccentrically compressed columns. The test specimens were carried out using a specially designed set-up. The test phenomena, stress-strain curves in cross section, load-displacement curves, rotation-displacement curves, and bearing capacity of the columns were obtained. The results were applied to validate the accuracy of the Direct Strength Method (DSM) in current specifications, as well as to evaluate the Effective Width Method (EWM).

ARTICLE HISTORY

Received: 13 August 2019
 Revised: 22 January 2020
 Accepted: 23 January 2020

KEYWORDS

Bearing capacity;
 Lipped channel columns;
 Mechanical properties;
 Stainless steel;
 Direct Strength Method

Copyright © 2020 by The Hong Kong Institute of Steel Construction. All rights reserved.

1. Introduction

Stainless steel materials have several advantages, such as attractive appearance, easy maintenance, and strong corrosion resistance [1]. In recent years, stainless steel has shown great prospects in a wide variety of structural applications and becomes a new favorite of many structural engineers and architects. However, the design methods and specifications for stainless steel structures are not perfect, and the section shape and size of a member has not been fully normalized. Moreover, the stress-strain curve of stainless steel is non-linear, which greatly differs from carbon steel. The design methods and rules for carbon steel cannot directly be applied to stainless steel. Therefore, the design methods of stainless steel columns require further study.

The cold-formed thin-walled members with open section (such as lipped channel section) are highly prone to several buckling modes, namely local, overall and distortional buckling, and interactions involving the three buckling modes. At present, a considerable amount of research effort was devoted to stainless steel columns experiencing local and global buckling, but the available literature on distortional buckling is much scarcer [2, 3]. Kwon and Hancock [4, 5] conducted extensive experiments on cold-formed columns with different sections, and the results show that distortional buckling tends to happen to the singly symmetric open section columns and is the controlling factor of bearing capacity. Tang and Young [6, 7] performed the column tests of cold-formed steel channels with complex stiffeners and inclined simple edge stiffeners, and the results show that the columns failing in distortional buckling presented the post-buckling strength and the interactions involving different buckling modes occurred in the columns. Many tests of lipped C- and Z- section beams experiencing distortional buckling were performed and the DSM was proposed [8-11]. Becque and Rasmussen [12-15] studied the local and overall buckling of lipped C- and I- section stainless steel columns. The experimental research on the ultimate strength of lipped channel stainless steel stub columns under axial and eccentric compression is detailed in [16-19], in

which comparisons of the test results with the predictions of the codes were analysed. Some experimental as well as numerical researches on stainless steel lipped channel members experiencing distortional and overall flexural-torsional interaction are reported in [20, 21]. For the stainless steel lipped channel columns, DSM was proposed by Lecce and Rasmussen [22-24], but limited test results are available.

In this paper, material properties were obtained according to 14 flat and corner tensile coupon tests. Totally, 6 axially compressed lipped channel stainless steel columns and 18 eccentrically compressed columns were tested. The structural behavior and ultimate strength of stainless steel lipped channel members under eccentric and concentric compression was investigated in the experiments, which can provide test phenomena, stress-strain curves, load-displacement curves, rotation-displacement curves, and bearing capacity of the columns. The experimental results were compared with the prediction results of four design specifications, ASCE [25], EC3 [26], AISI [27] and AS/NZS [28].

2. Material properties

Material tensile tests were conducted to determine the mechanical properties of austenitic AISI304 (EN1.4301) stainless steel in the flat and corner regions. The flat and corner coupons were cut from the lipped channel stainless steel column, with the thickness of 2.0 mm (0.079 in.) and 3.0 mm (0.118 in.), respectively. The flat and corner tensile coupons were tested in direction of rolling.

2.1. Tests of flat coupons

The flat coupons were divided into two groups according to the thickness of the coupons, and each group included 3 coupons, as shown in Table 1. The flat tensile coupons were tested at a strain rate of 0.5 mm/min (0.020 in./min.).

Table 1
 Number and dimensions of flat tensile coupons

Group	Number	Thickness (mm)	Measured Dimensions (mm)		Group	Number	Thickness (mm)	Measured Dimensions (mm)	
			Thickness	Width				Thickness	Width
1	CT-2-1	2.0	1.84	12.52	2	CT-3-1	3.0	2.78	12.54
	CT-2-2	2.0	1.84	12.53		CT-3-2	3.0	2.79	12.53
	CT-2-3	2.0	1.84	12.54		CT-3-3	3.0	2.78	12.53

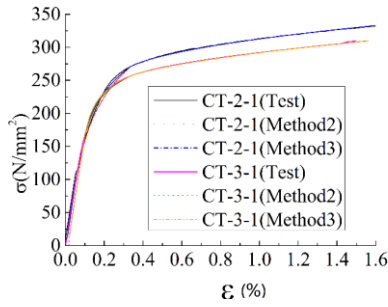
The tensile tests indicate that the stainless steel has a high elongation and smooth fracture surface. Table 2 gives the results of the flat tensile coupons. For coupon CT-3-3, the stress and tension were not collected

synchronously. Thus, the mechanical property could not be obtained. The stress-strain curves obtained from the flat tensile coupons are given in Fig. 1. For each flat coupon, there are three σ - ϵ curves in Fig. 1, obtained from the

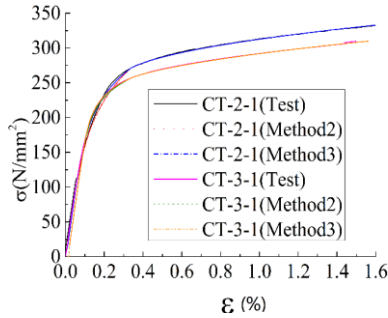
following methods: (1) Method 1: fitting the curves depending on the test data; (2) Method 2: drawing the σ - ε curves on the basis of the 2-stage model (Eq. (1)) [29]; (3) Method 3: drawing the σ - ε curves on the basis of the 2-stage model, but replacing index n with n_f (according to the tensile results). The comparison of the curves in Fig. 1 indicates that the curves from Method 3 are consistent with the test results.

$$\varepsilon = \begin{cases} \frac{\sigma}{E_0} + 0.002 \left(\frac{\sigma}{\sigma_{0.2}} \right)^n & \sigma < [0, \sigma_{0.2}] \\ \frac{\sigma - \sigma_{0.2}}{E_0} + \left(\varepsilon_{11.0} - \varepsilon_{10.2} - \frac{\sigma_{1.0} - \sigma_{0.2}}{E_{0.2}} \right) \left(\frac{\sigma - \sigma_{0.2}}{\sigma_{1.0} - \sigma_{0.2}} \right)^{n_{0.2,1.0}} + \varepsilon_{10.2} & \sigma < [\sigma_{0.2}, \sigma_u] \end{cases} \quad (1)$$

where $\sigma_{0.2}$ is the 0.2% proof stress, $\varepsilon_{10.2}$ is the total strain at the 0.2% proof stress, $\sigma_{1.0}$ is the 1.0% proof stress, $\varepsilon_{11.0}$ is the total strain at the 1.0% proof stress, E is the Young's modulus, $n_{0.2,1.0} = 12.255(E_{0.2}/E_0)(\sigma_{1.0}/\sigma_{0.2}) + 1.037$ [29] is the second strain hardening exponent, $E_{0.2}$ is the tangent modulus at the 0.2% proof stress, n is the strain hardening exponent.



(a) Coupons CT-2-1 and CT-3-1



(b) Coupons CT-2-2 and CT-3-2

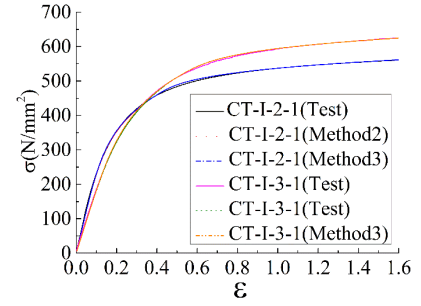
Fig. 1 σ - ε curves of flat coupon tests

2.2. Tests of corner coupons

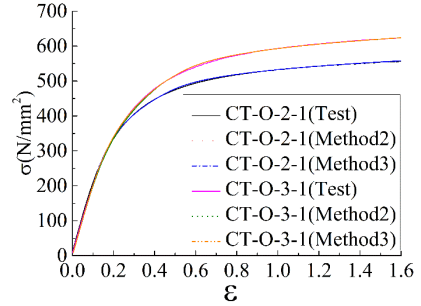
The corner coupons were divided into two groups according to the coupon thickness, and each group includes 4 coupons, as shown in Table 3. These corner coupons were tested in pairs (Part A and Part B shown in Table 3) to avoid eccentric loading. Table 4 gives the results of the flat tensile coupons, and the test data shows that the elongations of corner coupons are more than 20% but lower than those of flat coupons.

By comparing Tables 2 and 4, it shows that the cold-working significantly

enhance the strength of the corner coupons. The σ - ε curves of corner coupons were obtained in the same way as flat coupons. The measured σ - ε curves of the corner coupons are shown in Fig. 2, which indicates that the σ - ε curves from Method 2 and 3 coincide with the measured curves.



(a) Coupons CT-I-2-1 and CT-I-3-1



(b) coupons CT-O-2-1 and CT-O-3-1

Fig. 2 σ - ε curves of corner coupon tests

3. Distortional buckling tests

3.1. Section design

The failure modes of lipped channel columns are substantially determined by the elastic buckling load, which is related to the section size, length and boundary condition. The CUFSM software [30] was adopted to select cross sections failing in distortional buckling, and elastic buckling curve for a particular section was obtained, as presented in Fig. 3.

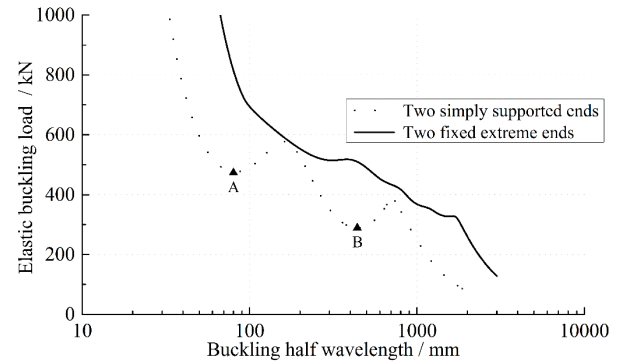


Fig. 3 The relationship curve of elastic buckling load and half-wave length

Table 2

Mechanical properties of stainless steel in the flat regions

Group	Number	E_0 (N/mm ²)	$\sigma_{0.01}$ (N/mm ²)	$\sigma_{0.2}$ (N/mm ²)	n	n_f	$\sigma_{1.0}$ (N/mm ²)	$n_{0.2}$	$\varepsilon_{10.2}$	$\varepsilon_{11.0}$	σ_u (N/mm ²)
1	CT-2-1	199581	141.32	271.80	4.58	5.71	318.98	2.02	0.00338	0.01164	793.11
	CT-2-2	206830	162.18	267.98	5.97	6.98	314.39	1.95	0.00328	0.01151	757.74
	CT-2-3	188981	160.01	267.04	5.85	6.62	314.03	2.18	0.00341	0.01163	751.37
	Average	198464	154.50	268.94	5.47	6.44	315.80	2.05	0.00336	0.01159	767.41
2	CT-3-1	193693	184.59	257.71	8.98	9.94	297.69	1.83	0.00334	0.01153	743.70
	CT-3-2	199254	163.38	254.61	6.75	7.77	298.02	1.87	0.00328	0.01149	757.18
	CT-3-3	-	-	-	-	-	-	-	-	-	-
	Average	196473	173.98	256.16	7.86	8.86	297.86	1.85	0.00331	0.01151	750.44

E_0 is the initial elastic modulus; σ_u is the ultimate strength; $\sigma_{0.01}$ is the strength with a residual deformation of 0.01%; $\sigma_{0.2}$ is the strength with a residual deformation of 0.2%; $\sigma_{1.0}$ is the strength with a residual deformation of 1.0%; $\varepsilon_{10.2}$ is the strain with the stress of $\sigma_{0.2}$; $\varepsilon_{11.0}$ is the strain with the stress of $\sigma_{1.0}$; n is the hardening index ($n = \ln(20)/\ln(\sigma_{0.2}/\sigma_{0.01})$), and n_f is the fitted hardening index by the method of least squares.

The continuous curve is for the fixed-ended columns and the dotted curve is for pinned-ended columns. The plot clearly shows two distinct minima to represent local buckling and distortional buckling (i.e., Point A and Point B) and finally an asymptotic portion representing overall buckling. However, the continuous curve does not show such distinct minima. Point A on the dotted curve represents the elastic local buckling load P_{cr1} , corresponding to a smaller half wavelength, and Point B represents the elastic distortional buckling load P_{cr2} , which is lower than the elastic local buckling load P_{cr1} for the columns. Thus, when the column length is appropriately selected, the overall buckling

will be avoided and the distortional buckling primarily determines the bearing capacity of the columns.

The elastic buckling analysis of lipped channel columns was carried out, including 21 sections in Chinese Code (GB50018-2002) [31], and 108 sections in Steel Framing Industry Association (SFIA), which was compiled according to AISI. Six sections were finally selected for the specimens, as presented in Table 5. The length of specimens was twice the distortional half-wavelength of the specimens.

Table 3
Number and dimensions of corner tensile coupons

Group	Corner coupons		Thickness (mm)	Weight (g)	Length (mm)	Section area (mm ²)	Density (kg/cm ³)
	Number	Compositions					
1	CT-I-2-1	Part A	2.0	31.66	200	20.02	7.92
		Part B	2.0	31.76	200	20.09	
	CT-I-2-2	Part A	2.0	31.89	200	20.14	
		Part B	2.0	31.53	200	19.91	
	CT-O-2-1	Part A	2.0	32.60	200	20.61	
		Part B	2.0	31.91	200	20.20	
CT-O-2-2	Part A	2.0	32.12	200	20.26		
	Part B	2.0	33.07	200	20.88		
2	CT-I-3-1	Part A	3.0	52.56	200	33.33	7.90
		Part B	3.0	52.41	200	33.20	
	CT-I-3-2	Part A	3.0	51.55	200	32.60	
		Part B	3.0	52.33	200	33.10	
	CT-O-3-1	Part A	3.0	53.38	200	33.86	
		Part B	3.0	55.32	200	35.10	
CT-O-3-2	Part A	3.0	53.06	200	33.56		
	Part B	3.0	53.84	200	34.08		

Part A and Part B represents two compositions cut from the symmetric corner regions of lipped C-section column.

Table 4
Mechanical properties of stainless steel in the corner regions

Group	Number	E_0 (N/mm ²)	$\sigma_{0.01}$ (N/mm ²)	$\sigma_{0.2}$ (N/mm ²)	n	n_f	$\sigma_{1.0}$ (N/mm ²)	$n_{0.2}$	$\epsilon_{10.2}$	$\epsilon_{1.0}$	σ_u (N/mm ²)
1	CT-I-2-1	244672	251.49	454.07	5.07	5.25	547.83	3.31	0.00386	0.01224	850.93
	CT-I-2-2	225135	254.78	440.86	5.46	5.55	533.42	2.92	0.00395	0.01238	835.42
	CT-O-2-1	206656	266.84	453.71	5.64	5.67	545.74	3.35	0.00420	0.01266	867.67
	CT-O-2-2	207870	249.24	435.33	5.37	5.48	526.66	3.34	0.00410	0.01255	-
	Average	221083	255.58	445.99	5.39	5.49	538.41	3.23	0.00402	0.01246	851.34
2	CT-I-3-1	185155	264.31	499.77	4.70	5.00	613.47	3.91	0.00470	0.01331	880.03
	CT-I-3-2	-	-	-	-	-	-	-	-	-	-
	CT-O-3-1	207971	242.38	493.04	4.22	4.58	610.68	3.75	0.00437	0.01294	895.74
	CT-O-3-2	-	-	-	-	-	-	-	-	-	-
	Average	196563	253.34	496.40	4.46	4.79	612.08	3.83	0.00453	0.01312	887.89

Table 5
Selected section and analysis results for specimens of column tests

Group	Section	Dimensions (mm)					P_{cr1} (kN)	P_{cr2} (kN)	l_{crd} (kN)	P_{cr1}/P_{cr2}	P_y (kN)	λ_d
		h	b	a	t	r						
1	C100x76x16x2	100	76	16	2	6	213.23	175.03	520	1.218	211.54	1.099
2	C100 x76x16x3	100	76	16	3	6	704.62	419.49	410	1.68	309.53	0.859
3	C92x64x16x2	92	64	16	2	6	230.43	202.7	450	1.137	184.15	0.953
4	C92x64x16x3	92	64	16	3	6	761.17	487.38	360	1.562	268.44	0.742
5	C64x42x13x2	64	42	13	2	6	340.66	244.31	270	1.394	117.38	0.693
6	C64x42x13x3	64	42	13	3	6	-	599.31	210	-	168.29	0.530

P_{crd} is the elastic distortional buckling load, l_{crd} is the half wavelength of elastic distortional buckling, P_y is the elastic yield load, and λ_d is the slenderness ratio of distortional buckling.

3.2. Test specimens

A total of 24 columns, including 6 axially compressed columns and 18 eccentrically compressed columns, were tested. The columns are presented in Fig. 4, the number and dimensions are detailed in Table 6. The symbolic meanings in Table 6 are shown in Fig. 5. To ensure uniform compression and prevented the top and bottom edges from localized failure, a 20 mm end plate was welded at both ends. The end plate material is Q235 steel.

The specimens were split into two groups according to the direction of eccentric load, that is negative or positive eccentricity, as shown in Fig. 6. The

eccentricity e takes a positive sign when the load is toward the lip; the eccentricity e takes a negative sign when the load is toward the web. Fig. 7 shows six types of stress distribution states, corresponding to the Code A-F specimens in Table 6: (1) Code A, the stress distribution is $\sigma_1 = 0.5\sigma_2$, as shown in Fig. 7 (a), where σ_1 represents the compressive stress at web-flange junction and σ_2 represents the compressive stress at the flange-lip junction; (2) Code B, the stress distribution is $\sigma_2 = 0.5\sigma_1$, as given in Fig. 7 (b); (3) Code C, the stress distribution is $\sigma_1 = 0$, as shown in Fig. 7 (c); σ_2 is the compressive stress; (4) Code D, the stress distribution is $\sigma_2 = 0$, as shown in Fig. 7 (d); σ_1 is the compressive stress; (5) Code E, the stress distribution is

$\sigma_1 = -0.125\sigma_2$, as shown in Fig. 7 (e); σ_1 is the tensile stress and σ_2 is the compressive stress; (6) Code F, the stress distribution is $\sigma_2 = -0.125\sigma_1$, as shown in Fig. 7 (f); σ_1 is the compressive stress and σ_2 is the tensile stress. Code A, C and E specimens represent the positive eccentric compression specimens, and Code B, D, and F represent the negative eccentric compression specimens.

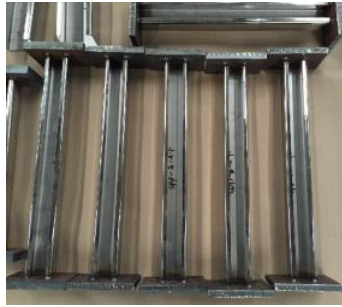


Fig. 4 Processed specimens

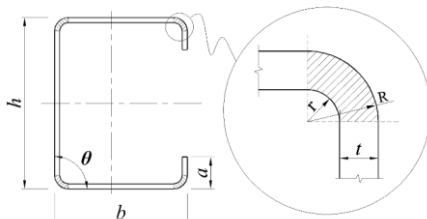


Fig. 5 Geometric parameters of lipped C section

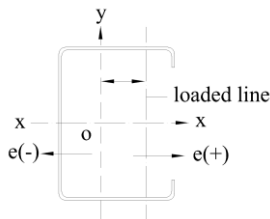


Fig. 6 Eccentric positions and directions of test load

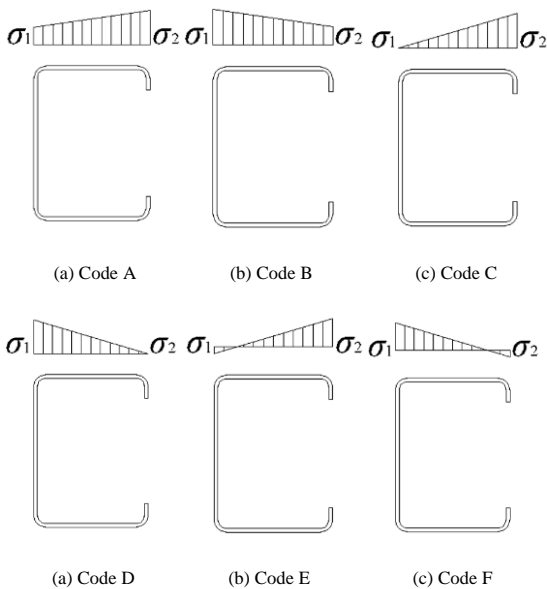


Fig.7 Stress distribution of cross section under different eccentric loads

3.3. Initial imperfection

The initial imperfections have a noticeable impact on the ultimate

strength of stainless steel lipped channel columns. Therefore, the initial imperfections were measured along 9 parallel lines for each cross-section. 3 lines on the upper flange (points A-1, A-2 and A-3), 3 lines on the web (points A-4, A-5 and A-6), and 3 lines on the lower flange (points A-7, A-8 and A-9), as shown in Fig. 8.

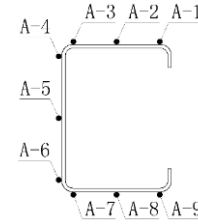


Fig. 8 Layout of measuring point for initial imperfection

The initial imperfections at the ends of the specimens are fairly higher than that in other regions because of the thermal properties and the effects of welding. They are not widely representative. Fan et al. [16] suggested deleting the data of two points close to the ends of the members. The initial imperfection curves of the specimens are presented in Fig. 9. The maximum amplitudes of the recorded initial imperfections are detailed in Table 7.

3.4. Test setups and measuring point distribution

The test setups include displacement meters, an RSA-600 electronic universal testing machine, and a TDS303 data logger, etc. All columns adopted pin-ended boundary conditions at the minor axis. The RSA-600 electronic universal testing machine is equipped with a servo control system, which can realize the infinitely variable speed movement of the beam in the range of 0.1~200mm/min. To accurately simulate the pin-ended boundary conditions, an improved loading system was designed, which primarily consisted of the hinged supports and holding devices, as given in Fig. 10 (a)-(c).

22 strain gauges were arranged at mid-height section of each specimen, which allowed the determination of the variation of stresses in the cross section, and the layout is shown in Fig. 11. The numbers of brackets in Fig. 11 represent the codes of strain gauges on the inner surface of the cross section. The axial displacement and end rotation were measured by eight displacement meters located at the corners of end plates to measure, as shown in Fig. 12 (a), and five displacement gauges were positioned at mid-height of the specimens, as given in Figs. 12 (b) and (c). Three displacement gauges were arranged at the web to measure the deformation of web and the overall lateral displacement. The other two were respectively positioned at the left and right flanges near the flange-lip junction for measuring the deformation of the flange.

Loaded with force control during the initial loading period, the loading rate is 0.5mm/min. After the load reaches 60% of the estimated strength of the columns, displacement control was adopted. If the load drops to 80% of the ultimate bearing capacity, the test terminated.

3.5. Test phenomena

3.5.1. Axially loaded columns

During the tests of columns under axial compression, two buckling modes were observed. One is distortional buckling (specimens SPZ-1 to SPZ-4), and the other is distortional-overall interaction (specimens SPZ-5 and SPZ-6). Specimens SPZ-2 and SPZ-6 were taken as examples.

For specimen SPZ-2, the phenomena and failure process are summarized as follows: For relatively small loads, there was only small axial compression deformation and no other obvious phenomena occurred in the specimen, as shown in Fig. 13 (a). As the load climbed, the both side flanges of the specimens began to rotate around the web-flange junction and the support end plates rotated. When the load was close to its bearing capacity, the flange involved outward flange-lip motions at the top end and the flange involved inward flange-lip motions at the bottom end, respectively, as given in Fig. 13 (b). Eventually, when the load passed its bearing capacity, the deformation of flanges and the rotation angle of two end plates increased rapidly with the decrease of load. The phenomenon and failure process of specimen SPZ-2 under different loads are given in Fig. 13 (a)-(c). The distortional buckling of specimen SPZ-2 before and after unloading is respectively illustrated in Figs. 13 (d) and (e). As can be seen in Fig. 13, (1) there was distinct distortional buckling when the specimen SPZ-2 failed; (2) two distortional half-waves

occurred in the specimen SPZ-2; (3) after unloading, distortional buckling presented an apparent rebound deformation.

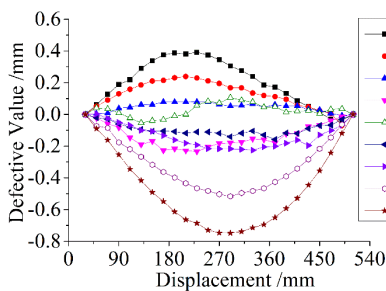
Table 6
Number and measured dimensions of specimens

Group	Number	Section type	h (mm)	b_1 (mm)	b_2 (mm)	a_1 (mm)	a_2 (mm)	t (mm)	l (mm)	r (mm)	θ_1	θ_2	A (mm ²)
Axially compressed columns	SPZ-1	C100×76×16×2	100.18	75.98	75.86	15.90	16.01	2.78	1039.27	6	89.1	88.3	723.14
	SPZ-2	C100×76×16×3	100.17	76.93	76.43	15.45	15.85	2.78	818.63	6	89.6	89.4	725.64
	SPZ-3	C92×64×16×2	92.38	65.07	64.81	15.34	15.91	2.78	898.73	6	88.9	88.1	638.57
	SPZ-4	C92×64×16×3	92.15	64.69	64.40	15.88	16.00	2.78	718.73	6	91.4	87.2	637.49
	SPZ-5	C64×42×13×2	63.85	42.45	42.90	13.10	13.00	2.78	538.67	6	88.6	90.1	421.15
	SPZ-6	C64×42×13×3	64.24	42.54	42.36	13.16	12.97	2.78	420.23	6	88.4	90.8	421.07
Eccentrically compressed columns	SPP-1-A	C100×76×16×2	100.64	76.94	76.99	16.62	16.3	1.84	1039.40	6	88.6	88.5	493.58
	SPP-1-B		100.17	76.45	77.23	15.85	15.91	1.84	1038.97	6	87.9	89.1	490.12
	SPP-1-C		100.13	76.69	76.84	15.95	15.99	1.84	1038.33	6	90.0	88.2	490.10
	SPP-1-D		100.59	77.04	76.66	16	16.33	1.84	1039.07	6	89.4	88.3	491.98
	SPP-1-E		100.49	76.43	76.40	15.71	16.12	1.84	1039.03	6	89.4	88.8	489.27
	SPP-1-F		100.44	76.83	76.09	15.78	15.96	1.84	1038.67	6	89.7	88.1	489.18
	SPP-2-A	C92×64×16×2	92.35	64.67	65.20	16.01	15.77	1.84	898.53	6	88.3	89	431.96
	SPP-2-B		92.05	64.47	65.22	16.03	15.93	1.84	899.00	6	90.2	89.4	431.41
	SPP-2-C		92.48	64.8	64.15	16.29	15.72	1.84	899.57	6	88.0	87.8	430.93
	SPP-2-D		92.22	64.91	64.54	16.14	15.91	1.84	898.57	6	89.0	89.4	431.44
	SPP-2-E		92.18	64.28	64.98	15.88	15.97	1.84	898.17	6	88.1	90.2	430.65
	SPP-2-F		92.08	64.36	64.89	15.8	16.09	1.84	898.33	6	86.6	92.1	430.52
	SPP-3-A	C64×42×13×2	64.06	42.61	42.40	13.21	12.92	1.84	539.03	6	89.7	89.9	286.97
	SPP-3-B		63.65	42.56	42.58	13.11	12.82	1.84	538.60	6	89.9	89.4	286.08
	SPP-3-C		64.06	42.48	42.52	13.28	13.26	1.84	538.07	6	87.8	88.8	287.70
	SPP-3-D		64.05	42.46	42.45	13.31	13.27	1.84	538.73	6	88.6	88.9	287.59
	SPP-3-E		63.69	42.47	42.55	13.25	13.31	1.84	537.83	6	88.3	91.4	287.09
	SPP-3-F		63.98	42.59	32.46	12.88	12.99	1.84	538.60	6	89.4	88.7	268.01

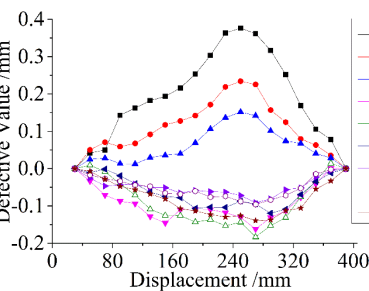
h is height of lipped C section; b_1 and b_2 are separately upper and lower flange widths; a_1 and a_2 are separately upper and lower lips widths; t is thickness of lipped C section; l is length of specimen; r is the internal radius of corner region on cross section; θ_1 and θ_2 are separately the angle between the web and upper and lower flange; A is the section area.

Table 7
Measured initial imperfection values of specimens

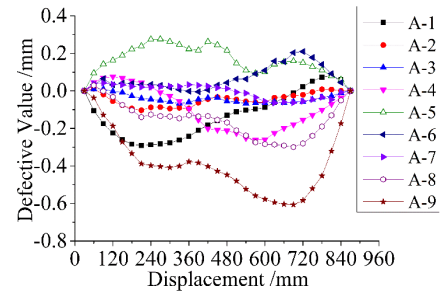
Number	Section	Imperfection position	Measured value (mm)	Number	Section	Imperfection position	Measured value (mm)
SPZ-5, SPP-3-A (B/C/D/E/F)	C64×42×13×2	Center of the web	0.1059	SPZ-6	C64×42×13×3	Center of the web	0.1830
		Flange-lip junction	0.7485			Flange-lip junction	0.3766
SPZ-3, SPP-2-A (B/C/D/E/F)	C92×64×16×2	Center of the web	0.2626	SPZ-4	C92×64×16×3	Center of the web	0.3230
		Flange-lip junction	0.6066			Flange-lip junction	0.8445
SPZ-1, SPP-1-A (B/C/D/E/F)	C100×76×16×2	Center of the web	0.2417	SPZ-2	C100×76×16×3	Center of the web	0.9477
		Flange-lip junction	1.0826			Flange-lip junction	0.7056



(a) C64×42×13×2



(b) C64×42×13×3



(c) C92×64×16×2

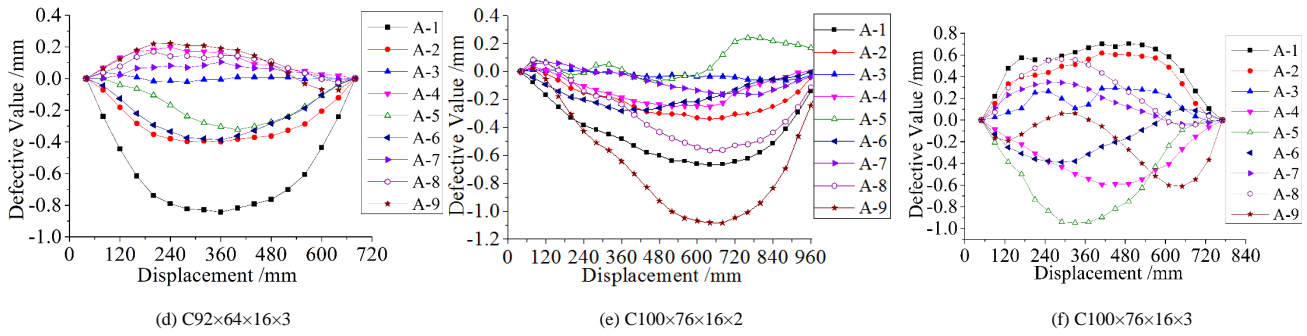


Fig. 9 Initial imperfection curves of specimens

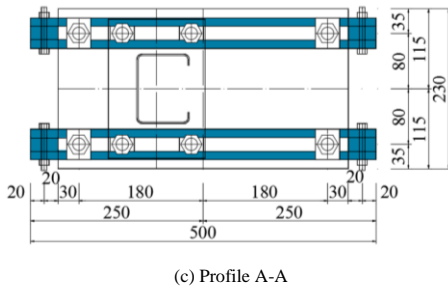
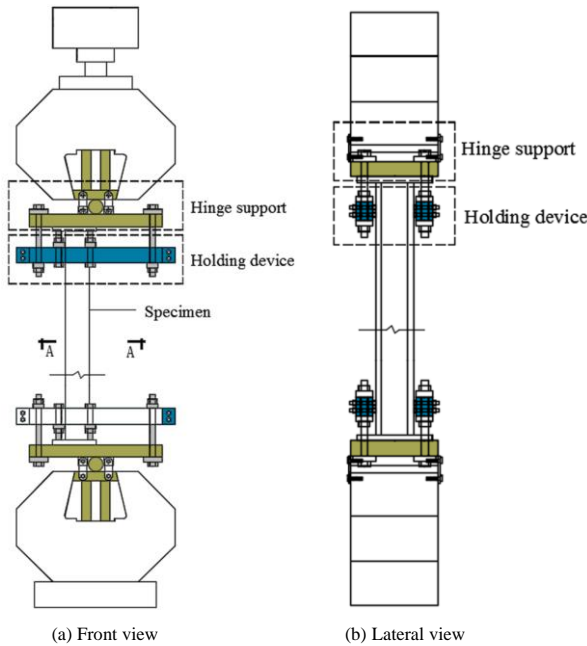


Fig. 10 Improved loading system

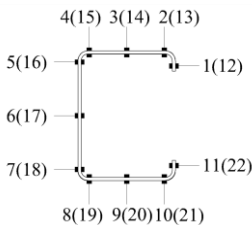


Fig. 11 Layout of strain gauges

For specimen SPZ-6, the failure procedure was summarized as follows: when the load is small, there was only slight axial deformation and no other obvious phenomena occurred in the specimen, as shown in Fig. 14 (a). As the load climbed, two end plates began to rotate, and overall buckling occurred in the specimen. Then a relatively large lateral displacement appeared at the mid-height of the specimen. When the load reached its ultimate bearing capacity, the flange involved outward flange-lip motions at the mid-height of

the column, and a large rotation occurred at the bottom end plate, as shown in Figs. 14 (b). Subsequently, with the rapid decrease of the test load, the distortional-overall interaction became rather apparent until the failure of the column, as pictured in Fig. 14(c). The distortional-overall interaction of SPZ-6 is respectively illustrated in Fig. 14 (d) and (e). The Fig. 14 shows that: (1) distortional-overall interaction occurred in the specimen SPZ-6; (2) the flange involved outward flange-lip motions at the mid-height of the column; and (3) a distortional half-wave was observed in the specimen.

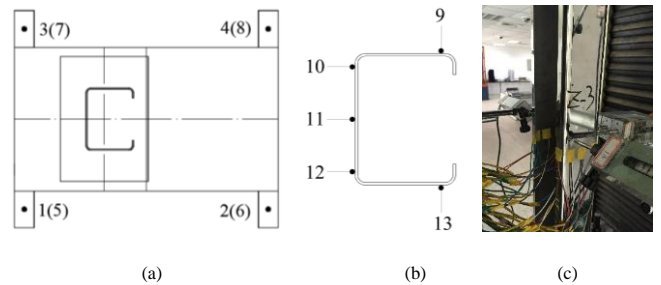


Fig. 12 Layouts of displacement gauges: (a) axial displacement (b) lateral displacement (c) lateral displacement at the mid-height of the specimen

3.5.2. Positive eccentrically loaded specimens

For the positive eccentrically loaded specimens SPP-1-A/C/E, SPP-2-A/C/E and SPP-3-A/C/E, the failure process and phenomena are like those of columns under axial compression. The failure modes of the columns under positive eccentric compression are given in Fig. 15 (a)-(c). Fig. 15 shows: (1) distortional buckling occurred in the specimens under positive eccentric compression, and at least a half-wave of distortional buckling was observed; (2) there were differences between the wave shapes of different specimens; for specimens SPP-1-C/E and SPP-2-A/C, there are two distortional half-waves, and the flange involved outward flange-lip motions at top end the flange involved inward flange-lip motions at bottom end; whereas the wave shapes of buckling are just the opposite for specimens SPP-1-A, SPP-2-E and SPP-3-A; and (3) for the specimen SPP-3-C/E, a half-wave of distortional buckling observed at mid-height of the specimen, and the flange involved outward flange-lip motions.

3.5.3. Negative eccentrically loaded specimens

For the negative eccentrically loaded specimens SPP-1-B/D/F, SPP-2-B/D/F and SPP-3-B/D/F, the failure process and phenomena are different from those of the columns under positive eccentric compression. The specimen SPP-1-B was chosen as an example.

For relatively small loads, there was only the slight axial deformation, and no other observable phenomena occurred in the specimen, as shown in Fig. 16 (a). With the increase of the load, local buckling began to appear in the web and flanges, as given in Fig. 16 (b). When the load was up to the bearing capacity, apparent local buckling was observed in the flanges and web, as given in Fig. 16 (c). Finally, when the load passed its bearing capacity, observable local buckling at mid-height of the specimens developed rapidly, which led to the damage of the columns, as given in Fig. 16 (d). The buckling modes of the members SPP-1-B before and after unloading are illustrated in Figs. 16 (e) and (f), respectively.

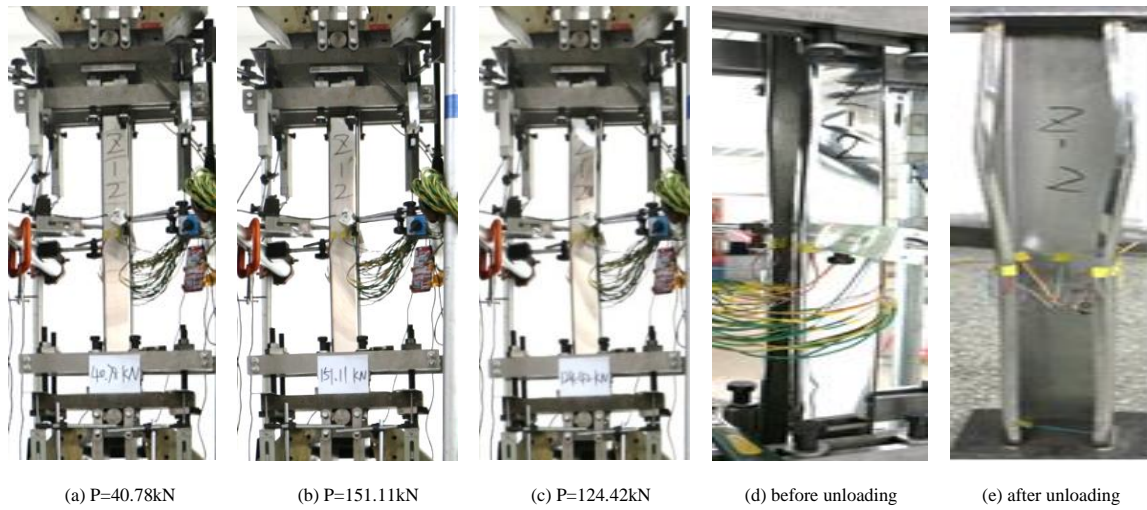


Fig. 13 Failure process of axially loaded specimen SPZ-2

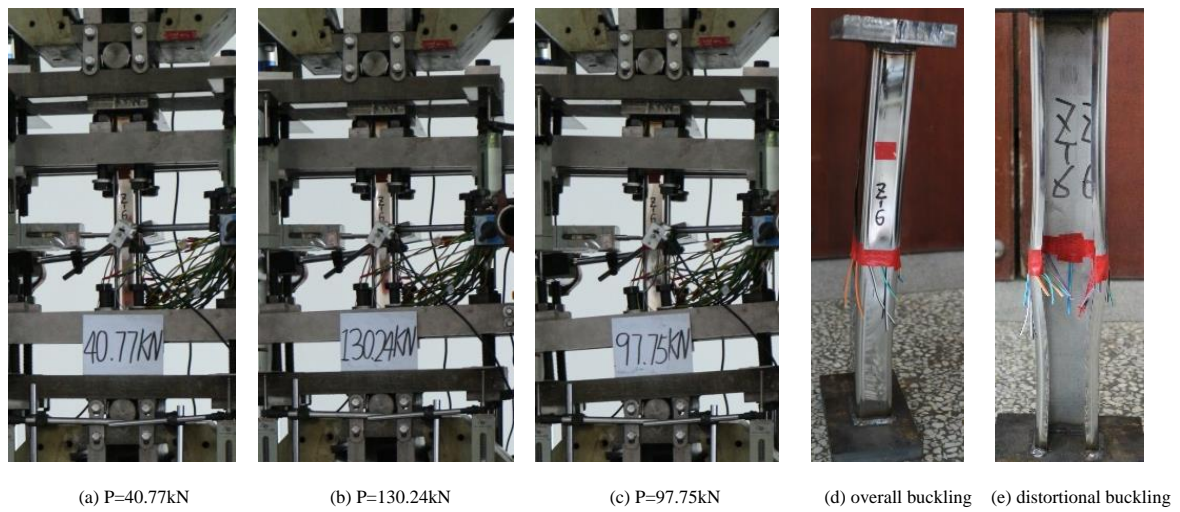


Fig. 14 Failure process of axially loaded specimen SPZ-6



Fig. 15 Failure of positive eccentrically loaded specimens

3.6. Experimental results

3.6.1. Load-axial displacement curves

The load-axial displacement curves of the column under axial and eccentric compression are shown in Fig. 17, which indicates that: (1) the load-axial displacement curves of the columns have a similar pattern, and the axial displacement of the column grows linearly with the increase of load at initial stage; (2) For the specimens under eccentric compression, the ultimate

bearing capacities of the specimen reduce gradually with the increase of eccentricity; and (3) its ductility is related to the eccentric direction and the eccentricity; for specimens with same eccentric direction (such as SPP-1-A/C/E or SPP-1-B/D/F), the ductility is enhanced with the increase of eccentricity; for the specimens with different eccentric directions (such as SPP-1-A and SPP-1-B), the ductility of the specimens with positive load eccentricity is larger than that of the specimens with negative load eccentricity.

3.6.2. Load-lateral displacement curves

Fig. 18 shows the load-lateral displacement curves of the columns subjected to concentric and eccentric compression. The conclusions according to Fig. 18 are as follows: (1) for the specimens SPZ-1, the deformation of flange firstly appeared, and then the overall buckling was observed in the specimen, as given in Fig. 18 (a); for the specimens SPZ-6, the overall buckling firstly figured, and then the deformation of flange appeared, as shown in Fig. 18 (c); for other specimens under axial compression, the deformation of the flange as well as overall buckling were simultaneously observed at the initial stage, as given in Fig. 18 (b); and (2) the deformation of flanges is outward, and the web is inward, as shown by specimens SPZ-6 and SPP-3-A; and vice versa, as shown by specimens SPZ-1, SPZ-3, SPP-1-E, and SPP-3-E.

3.6.3. Strain distribution on the cross-section

The layout of strain gauges at the mid-height of the specimen are shown in Fig. 11. The strain distribution of the members under axial compression is shown in Fig. 19 (a)-(c), and the strain distribution of the members under eccentric compression is presented in Fig. 19 (d)-(i).

For the specimens subjected to axial compression, it can be seen from Fig. 19 (a)-(c): (1) for specimen SPZ-1, the strain distribution showed an M shape before the load is up to its ultimate value, which is similar to the strain

distribution of specimens SPZ-2~SPZ-4 when the load reached its limit load, as shown in Fig. 19 (a); (2) for specimens SPZ-2, SPZ-3 and SPZ-4, before the load up to its limit load, the strain increased as the increase of the load, and the increasing rate of strain in the flanges is larger than that in the web or lip; the strain distribution shown a W shape, as shown in Fig. 19 (b); when the load up to its limit load, the strain value in web and lip was rarely enhanced, but strain value in the flanges was increased further; (3) for the specimens SPZ-5 and SPZ-6, before the test load reached the ultimate value, the compressive strain on the cross section remains substantially linear, indicating that the global buckling occurred and the distortional buckling was not obviously observed; when the load reached its limit load, the strain in the lip was increased rapidly, showing that the distortional buckling was gradually observed in the specimen, as shown in Fig. 19 (c).

It can be seen from Fig. 19 (d)-(i): (1) for the specimens under positive eccentric compression, the strain distribution of the cross section is similar to that of the specimens subjected to axial compression with the same section, and the strain in the web is always tensile strain; (2) for the specimens under negative eccentric compression, the strain distribution of cross section is basically consistent, such as the specimens SPP-1-F, SPP-2-F and SPP-3-F; and (3) the tensile strain in the lips of the specimen SPP-3-F is larger than that of the specimens SPP-1-F and SPP-2-F, indicating the specimen SPP-3-F failing in overall buckling is more obvious.

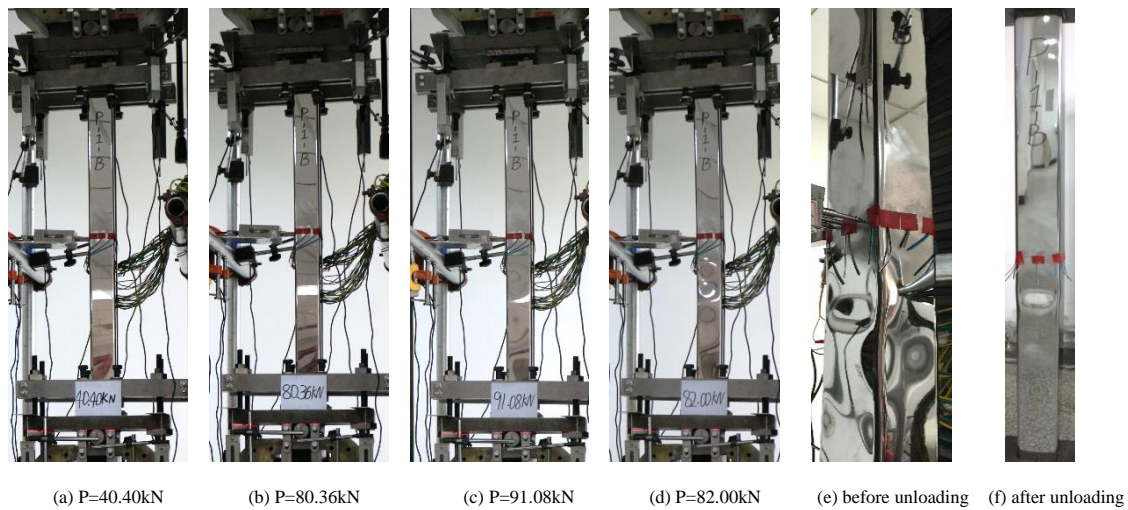


Fig. 16 Failure process of negative eccentrically loaded specimen SPP-1-B

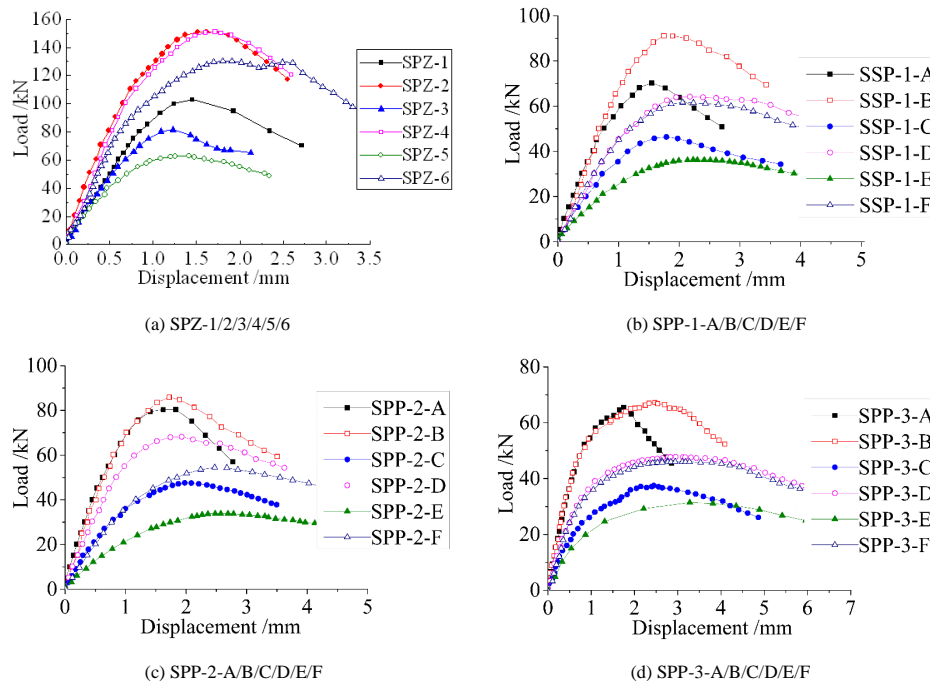


Fig. 17 Load-axial displacement curves of specimens

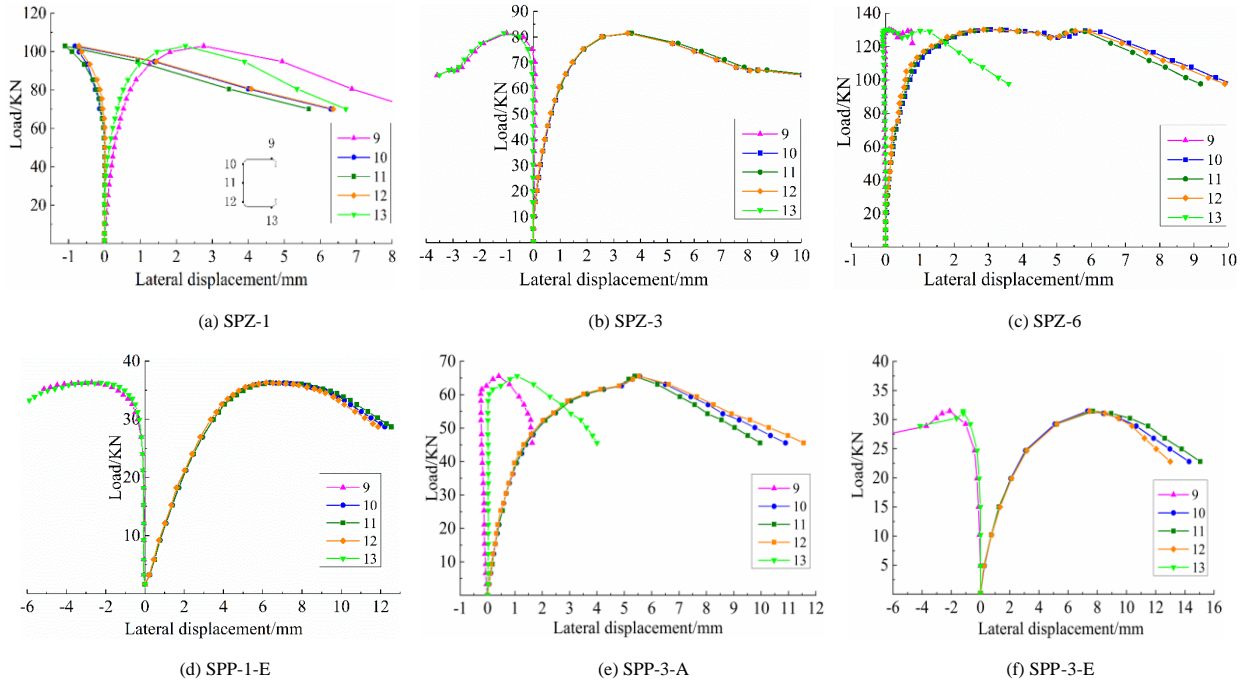


Fig. 18 Load-lateral displacement curves of specimens

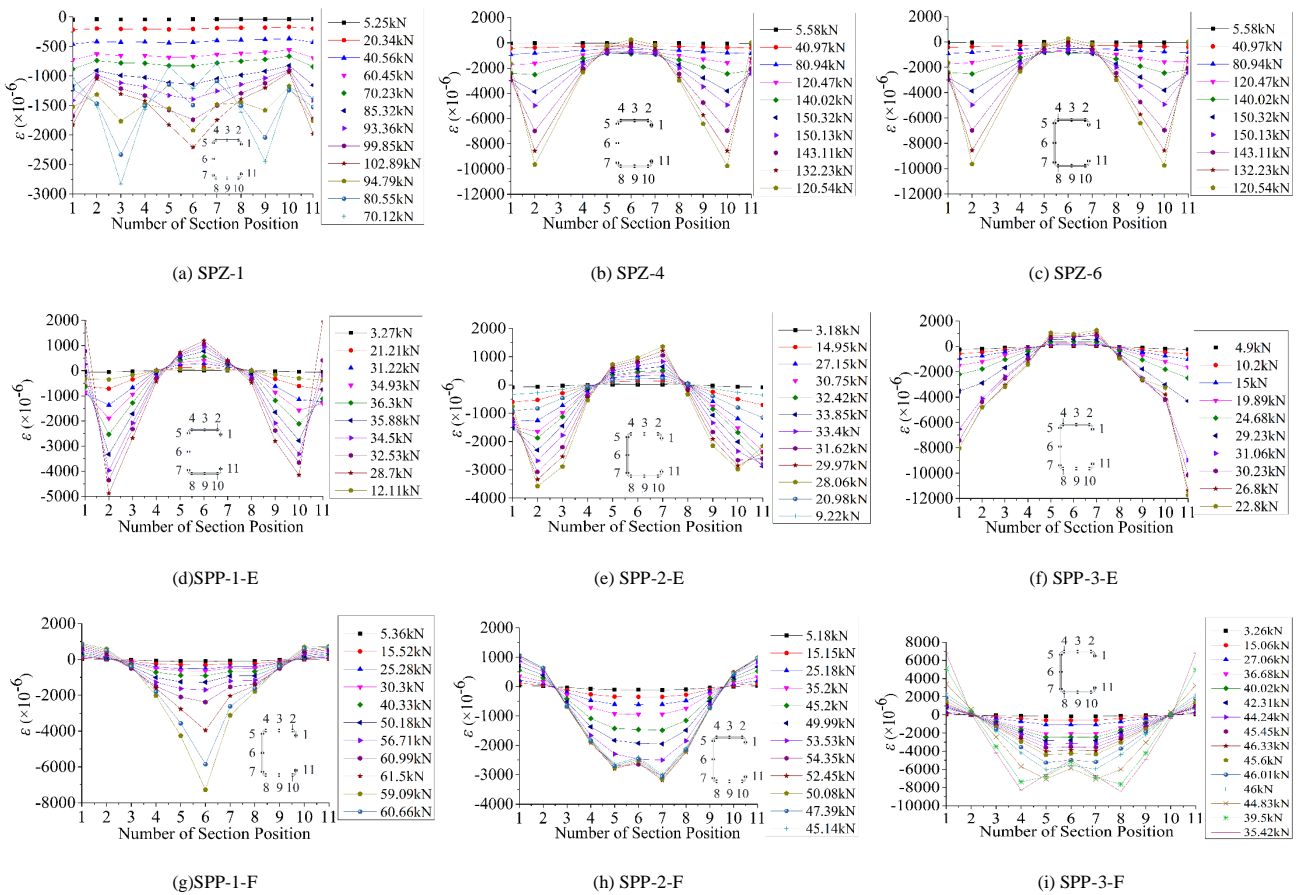


Fig. 19 Strain distribution at the mid-height of specimens

3.6.4. Bearing capacity and failure modes

The test results and the failure modes of the members are detailed in Table 8. The difference between the theoretical and the practical value of eccentricity was generated due to the installation of the test setup and the manufacturing of the specimens. The practical value of eccentricity was deduced from the stress distribution at the mid-height section of each specimen.

As presented in Table 8, for the specimens subjected to axial compression, the distortional-overall interaction occurred in the specimens SPZ-5 and

SPZ-6, and there is only distortional buckling in other specimens; the distortional buckling and distortional-overall interaction were observed in the specimens under positive eccentric compression; the local buckling and local-global interaction were presented in the specimens under negative eccentric compression.

4. Comparisons of test results and code results

For stainless steel columns, to determine the bearing capacity of

distortional buckling, two methods were adopted, including effective width method (EWM) and DSM. In the EWM, the distortional buckling is treated as a special local buckling, and the influence of distortional buckling on the bearing strength of the columns is considered by decreasing the buckling coefficient of plate or reducing the section thickness. The calculation will be very complicated when the section form of component becomes more and more complex. In the DSM, the ultimate bearing capacity is determined according to the relationship between the elastic critical buckling load and the ultimate strength. Comparisons between the experimental values and the predictions by above two methods were performed.

4.1. Comparisons of test results with EWM results

EWM is available in current design codes including the EC3 and ASCE. For the axially loaded specimens SPZ-1~SPZ-6, the distortional buckling bearing capacities can be obtained by the EWM in the two design codes. The calculation results were compared with the test results, as shown in Table 9. P_T is the experimental value; P_{EC3} is the calculated value obtained from EC3; P_{ASCE} is the calculated value obtained from ASCE; DEV_T is the deviation

between test results and calculation results; and λ_d is the distortional buckling slenderness, determined by Eqs. (2) and (3).

$$\lambda_d = \sqrt{P_y/P_{crd}} \quad (2)$$

$$P_y = Af_y \quad (3)$$

where, P_{crd} is the elastic critical buckling strength; P_y is the yield bearing capacity; A is the section area of columns; and f_y is the yield strength.

The ratios of the calculation results obtained by EWM with the test results under different slenderness ratios λ_d are drawn in Fig. 20 (a). Table 9 and Fig. 20 (a) indicate that: (1) except for the specimen SPZ-1, the calculation results obtained from the two design codes are higher than the experimental values; (2) the ratios of the calculation results to the experimental values are greater than 1.0, and it indicates that the EWM is unsafe to calculate the distortional buckling strength for lipped channel members; and (3) the calculation results obtained from ASCE are greater than those from EC3.

Table 8

Bearing capacity and buckling modes of specimens

Number	Eccentricity (mm)		Buckling mode	Number of half-wave of distortional buckling	P_T (kN)
	Theoretical value	Practical value			
SPZ-1	0	0.41	D	2	102.89
SPZ-2	0	0.82	D	2	151.11
SPZ-3	0	2.47	D	2	81.53
SPZ-4	0	1.64	D	2	151.02
SPZ-5	0	2.01	D+F	2	62.76
SPZ-6	0	0.49	D+F	1	130.24
SPP-1-A	7.35	6.77	D	2	70.28
SPP-1-B	6.21	-5.49	L	—	91.08
SPP-1-C	26.43	26.71	D	2	46.40
SPP-1-D	-16.31	-18.98	L	—	64.20
SPP-1-E	37.29	36.52	D	2	36.30
SPP-1-F	-19.65	-20.48	L	—	61.66
SPP-2-A	6.26	5.09	D	2	80.38
SPP-2-B	-5.34	-5.02	L	—	85.90
SPP-2-C	22.60	22.16	D	2	47.60
SPP-2-D	-13.96	-13.71	L	—	68.22
SPP-2-E	31.92	35.50	D	2	33.85
SPP-2-F	-16.97	-19.51	L	—	54.44
SPP-3-A	4.02	4.56	D+F	2	65.56
SPP-3-B	-3.48	-3.29	L+F	—	67.21
SPP-3-C	14.31	16.56	D+F	1	37.50
SPP-3-D	-9.27	-9.45	L+F	—	47.82
SPP-3-E	19.90	21.31	D+F	1	30.13
SPP-3-F	-11.23	-11.70	L+F	—	46.04

D means distortional buckling, L means the local buckling, and F means overall buckling; P_T is the test result of ultimate bearing capacity of specimen.

4.2. Comparisons of test results with DSM results

Currently, DSM is available in AS/NZS and AISI. For the axially loaded specimens SPZ-1~SPZ-6 and the positive eccentrically loaded specimens SPP-1-A/C/E, SPP-2-A/C/E and SPP-3-A/C/E, the capacities in distortional buckling and distortional-overall interaction were obtained by the DSM in design codes, and comparison between the predictions and the experimental values was performed. The ultimate bearing capacity of stainless steel columns could be calculated by the DSM including in AISI (Eq. (4)) [27] and AS/NZS (Eq. (5)) [28], and the DSM equation (Eq. (6)) proposed by Lecce and Rasmussen [23, 24]. The comparisons of test results from this paper and calculation values obtained by the DSM are shown in Table 10. P_{AISI} , P_{AS} , and P_{LR} are the design strengths for AISI, AS/NZS, and DSM proposed by Rasmussen and Lecce.

$$\begin{cases} P_{nd} = P_y & \text{For } \lambda_d \leq 0.561 \\ P_{nd} = \left[1 - 0.25 \left(\frac{P_{crd}}{P_y} \right)^{0.6} \right] \left(\frac{P_{crd}}{P_y} \right)^{0.6} P_y & \text{For } \lambda_d > 0.561 \end{cases} \quad (4)$$

$$\begin{cases} P_{nd} = Af_y \left(1 - \frac{f_y}{4f_{od}} \right) & \text{For } f_{od} > \frac{f_y}{2} \\ P_{nd} = Af_y \left[0.055 \left(\sqrt{\frac{f_y}{f_{od}}} - 3.6 \right)^2 + 0.237 \right] & \text{For } \frac{f_y}{13} \leq f_{od} \leq \frac{f_y}{2} \end{cases} \quad (5)$$

$$\begin{cases} P_{nd} = P_y & \text{For } \lambda_d \leq 0.533 \\ P_{nd} = \left(\frac{0.8}{\lambda_d^{1.1}} - \frac{0.15}{\lambda_d^2} \right) P_y & \text{For } \lambda_d > 0.533 \end{cases} \quad (6)$$

where f_{od} is the elastic critical buckling stress, P_{nd} is the distortional buckling strength.

The ratios of the calculation results obtained by DSM with the test results under different slenderness ratios λ_d are drawn in Fig. 20 (b). The conclusions based on Table 10 and Fig. 20 (b) are as follows: (1) the calculation results obtained by the DSM are greater than the experimental values; (2) the DSM detailed in AS/NZS and AISI is primarily applied for calculating the strength of carbon steel or low yield point steel columns, and is inapplicable to the distortional buckling strength of stainless steel members in

compression; there are significant deviations between the test values and the DSM calculation results of design codes; (3) the load eccentricity has distinct influences on the distortional buckling bearing capacity of the columns under eccentric compression; and (4) for the stainless steel lipped channel members,

the DSM can predict the distortional buckling strength more accurately than the EWM.

Table 9

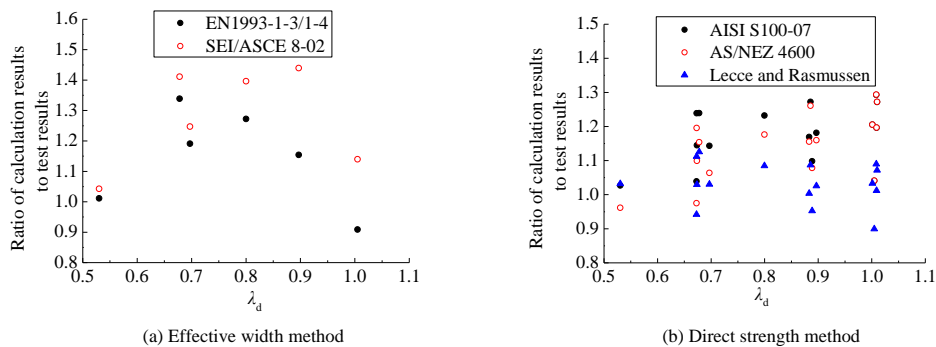
Comparisons of test results from this paper and calculation results obtained from effective width method

Number	λ_d	Test		European Code			American Specification		
		Eccentricity (mm)	P_T (kN)	P_{EC3} (kN)	DEV_T (%)	P_{EC3}/P_T	P_{ASCE} (kN)	DEV_T (%)	P_{ASCE}/P_T
SPZ-1	1.005	0.41	102.89	100.28	-2.54	0.97	117.29	14.00	1.14
SPZ-2	0.800	0.82	150.81	199.94	32.58	1.33	210.56	39.62	1.40
SPZ-3	0.897	2.47	81.53	102.09	25.22	1.25	117.35	43.94	1.44
SPZ-4	0.697	1.64	151.02	186.63	23.58	1.24	188.37	24.73	1.25
SPZ-5	0.678	2.01	62.76	87.26	39.03	1.39	88.57	41.12	1.41
SPZ-6	0.530	0.49	130.24	135.82	4.28	1.04	135.82	4.28	1.04
				Average	20.36	1.20	Average	27.95	1.28

Table 10

Comparisons of test results from this paper and calculation results obtained from direct strength method

Number	λ_d	Test		North American Specification			Australia Specification			Lecce and Rasmussen's method		
		Eccentricity (mm)	P_T (kN)	P_{AISI} (kN)	P_{AISI}/P_T	DEV_T (%)	P_{AS} (kN)	P_{AS}/P_T	DEV_T (%)	P_{LR} (kN)	P_{LR}/P_T	DEV_T (%)
SPZ-1	1.005	0.41	102.89	107.08	1.04	4.07	107.11	1.04	4.10	92.53	0.90	-10.07
SPZ-2	0.800	0.82	150.81	185.81	1.23	23.21	177.43	1.18	17.65	163.60	1.08	8.48
SPZ-3	0.897	2.47	81.53	96.34	1.18	18.17	94.57	1.16	15.99	83.62	1.03	2.56
SPZ-4	0.697	1.64	151.02	172.64	1.14	14.32	160.69	1.06	6.40	155.62	1.03	3.04
SPZ-5	0.678	2.01	62.76	77.77	1.24	23.91	72.41	1.15	15.38	70.64	1.13	12.55
SPZ-6	0.530	0.49	130.24	133.74	1.03	2.69	125.23	0.96	-3.85	134.39	1.03	3.19
SPP-1-A	1.001	6.77	70.28	84.72	1.21	20.54	84.73	1.21	20.56	72.62	1.03	3.33
SPP-1-C	1.009	26.71	46.40	55.51	1.20	19.62	55.54	1.20	19.69	46.96	1.01	1.20
SPP-1-E	1.009	36.52	36.30	46.93	1.29	29.29	46.95	1.29	29.35	39.56	1.09	8.97
SPP-2-A	0.889	5.09	80.38	88.25	1.10	9.79	86.67	1.08	7.83	76.57	0.95	-4.75
SPP-2-C	0.883	22.16	47.60	55.67	1.17	16.95	54.99	1.16	15.53	47.78	1.00	0.37
SPP-2-E	0.886	35.50	33.85	43.07	1.27	27.25	42.68	1.26	26.09	36.80	1.09	8.71
SPP-3-A	0.673	4.56	65.56	68.12	1.04	3.91	63.93	0.98	-2.48	61.75	0.94	-5.81
SPP-3-C	0.674	16.56	37.50	42.93	1.14	14.48	41.23	1.10	9.93	38.61	1.03	2.95
SPP-3-E	0.673	21.31	30.13	37.32	1.24	23.88	36.02	1.20	19.56	33.50	1.11	11.21
				Average	1.168	17.80	Average	1.135	14.66	Average	1.03	3.63

**Fig. 20** Ratios of calculation results to test results under different slenderness ratios

5. Conclusions

Experimental studies were performed on the lipped channel stainless steel columns under eccentric and concentric compression, and the test results were compared with the calculation results obtained by different design codes. It can be concluded as follows:

(1) The distortional buckling and distortional-overall interaction were observed in the members subjected to pure axial and positive eccentric compression, and the local buckling and local-overall interaction occurred in the columns under negative eccentric compression.

(2) For the specimens subjected to axial compression, the strain

distribution is uniform and almost horizontal at the initial loading period. With the increase of the test load, the strain in the middle web became lower while the strain at lip became higher.

(3) The strength of the specimens subjected to eccentric compression is gradually decreased with the increase of eccentricity, and the ductility of the specimens subjected to eccentric compression in the same direction is enhanced with the increase of eccentricity. For the eccentrically loaded columns in different directions, the ductility of the columns with positive load eccentricity is larger than that of the columns with negative load eccentricity.

(4) The calculation results obtained from EWM and DSM are higher than the experimental values. For lipped channel stainless steel columns, the DSM

can accurately predict the distortional buckling strength.

Acknowledgments

The writers are thankful to Prof. Benjamin W. Schafer and Dr. Shahabeddin Torabian at the Johns Hopkins University for offering ideas with

References

- [1] Waller G. and Cochrane D.J., "Stainless steel for durability, fire-resistance and safety", *Architecture Technique*, 9, 254-257, 2011.
- [2] Rasmussen K.J.R. and Hancock G.J., "Design of cold-formed stainless steel tubular members. I: Column", *Journal of Structural Engineering*, 119(8), 2349-2367, 1993.
- [3] Van den Berg G.J., "The effect of the non-linear stress-strain behaviour of stainless steel on member capacity", *Journal of Constructional Steel Research*, 54(1), 135-160, 2000.
- [4] Kwon Y.B. and Hancock G.J., "Tests of cold-formed channels with local and distortional buckling", *Journal of Structural Engineering*, 118(7), 1786-1803, 1992.
- [5] Yang D. and Hancock G.J., "Compression tests of high strength steel channel columns with interaction between local and distortional buckling", *American Society of Civil Engineers*, 130(12), 1954-1963, 2004.
- [6] Tang J. and Young B., "Column tests of cold-formed steel channels with complex stiffeners", *Journal of Structural Engineering*, 128(6), 737-745, 2002.
- [7] Tang J. and Young B., "Compression tests of channels with inclined simple edge stiffeners", *Journal of Structural Engineering*, 129(10), 1403-1411, 2002.
- [8] Schafer B.W., "Distortional buckling of cold-formed steel columns", Final Report to the American Iron and Steel Institute, Washington (DC), 2000.
- [9] Schafer B.W., "Local, distortional, and Euler buckling of thin-walled columns", *Journal of Structural Engineering*, 128(3), 289-299, 2002.
- [10] Yu C. and Schafer B.W., "Distortional buckling tests on cold-formed steel beams", *Journal of Structural Engineering*, ASCE, 132(4), 515-528, 2006.
- [11] Moen C.D. and Schafer B.W., "Experiments on cold-formed steel columns with holes", *Thin-Walled Structures*, 46(3), 1164-1182, 2008.
- [12] Becque J. and Rasmussen K.J.R., "Experimental investigation of local-overall interaction buckling of stainless steel lipped channel columns", *Journal of Constructional Steel Research*, 65(8-9), 1677-1684, 2009.
- [13] Becque J. and Rasmussen K.J.R., "Numerical investigation of local-overall interaction buckling of stainless steel lipped channel columns", *Journal of Constructional Steel Research*, 65(8-9), 1685-1693, 2009.
- [14] Becque J. and Rasmussen K.J.R., "Experimental investigation of the interaction of local and overall buckling of stainless steel I-columns", *Journal of Structural Engineering*, ASCE, 135(11), 1340-1348, 2009.
- [15] Becque J. and Rasmussen K.J.R., "Numerical investigation of the interaction of local and overall buckling of stainless steel I-columns", *Journal of Structural Engineering*, ASCE, 135(11), 1349-1356, 2009.
- [16] Fan S.G., Liu F., Zheng B.F., Shu G.P. and Tao Y.L., "Experimental study on bearing capacity of stainless steel lipped C section stub columns", *Thin-Walled Structures*, 83, 70-84, 2014.
- [17] Fan S.G., Tao Y.L., Zheng B.F. and Liu F., "Capacity of stainless steel lipped Channel stub column under axial compression", *Journal of Constructional Steel Research*, 103(12), 251-263, 2014.
- [18] Fan S.G., Zheng B.F., Liu M.J., Liu F. and Tao Y.L., "Direct strength method of capacity of stainless steel lipped C section stub columns", *Journal of Southeast University (Natural Science Edition)*, 44(6), 1246-1253, 2014.
- [19] Liu F., Theoretical and experimental investigations on the method of effective section of stainless steel lipped C stub columns, Master Thesis, School of Civil Engineering, Southeast University, 2012.
- [20] Rossi B., Jaspart J.P. and Rasmussen K.J.R., "Combined distortional and overall flexural-torsional buckling of cold-formed stainless steel sections: Experimental investigations", *Journal of Structural Engineering*, ASCE, 136(4), 354-360, 2010.
- [21] Rossi B., Jaspart J.P. and Rasmussen K.J.R., "Combined distortional and overall flexural-torsional buckling of cold-formed stainless steel sections: Design", *Journal of Structural Engineering*, ASCE, 136(4), 361-369, 2010.
- [22] Lecce M., Distortional buckling of stainless steel sections, PhD Thesis, University of Sydney, 2006.
- [23] Lecce M. and Rasmussen K.J.R., "Distortional buckling of cold-formed stainless steel sections: Experimental investigation", *Journal of Structural Engineering*, ASCE, 132(4), 497-504, 2006.
- [24] Lecce M. and Rasmussen K.J.R., "Distortional buckling of cold-formed stainless steel sections: Finite element modeling and design", *Journal of Structural Engineering*, ASCE, 132(4), 505-514, 2006.
- [25] ASCE, Specification for the Design of Cold-formed Stainless Steel Structural Members, American Society of Civil Engineers, SEI/ASCE8-90, Reston, Virginia, 2002.
- [26] EC3, Eurocode 3: Design of steel structures Part 1.4: General rules—supplementary rules for stainless steels, European Committee for Standardization, EN 1993-1-4, CEN, Brussels, 2006.
- [27] AISI, North American Specification for the design of cold formed steel structures: Appendix 1: Design of cold-formed steel structural members using the direct strength method, American Iron and Steel Institute, Washington (DC), 2004.
- [28] Australian/New Zealand Standard, Cold-formed steel structures, AS/NZS4600, Sydney, 2005.
- [29] Gardner L., A new approach to stainless steel structural design, PhD Thesis, Department of Civil and Environmental Engineering, Imperial College, London, 2002.
- [30] Li Z. and Schafer B.W., "Buckling analysis of cold-formed steel members with general boundary conditions using CUFSM: conventional and constrained finite strip methods", Proceedings of the 20th International conference: Special Conference on Cold-Formed Steel Structures, St. Louis, 2010.
- [31] National Standard of the People's Republic of China, Technical code of cold-formed thin-wall steel structures, GB50018-2002, Beijing, China planning press, 2002.

test rig. The research was sponsored by National Natural Science Foundation of China (No. 51878146 and No. 51378105), and National Key Research and Development Program of China (No. 2017YFC0703802). The authors also appreciate the financial supports from High level talents of "six talent peaks" in Jiangsu Province (No. JZ-001) and Qing Lan Project of Jiangsu Province (2016).